Further studies into the flow corrosion cathodic mass transfer kinetics of copper and nickel-aluminium bronze wall-jet electrodes

R.C. Barik[1,2], J.A. Wharton[1], RJK Wood[1] and K.R. Stokes[1,3]
[1] National Centre for Advanced Tribology (nCATS), Faculty of Engineering and Physical Sciences, University of Southampton, Highfield, Southampton, SO17 1BJ, UK.
[2] CSIR-Central Electrochemical Research Institute, Karaikudi, Tamil Nadu-63006, India.
[3]Platform Sciences Group, Dstl Porton Down, Salisbury, Wiltshire, SP4 0JQ, UK.

Abstract

This work has investigated the corrosion performance and mass transfer of oxygen on copper and nickel-aluminium bronze surfaces within a wall-jet flow cell assembly. Limiting currents of the dissolved oxygen mass-transfer kinetics as a function of volume flow rate at a wall-jet electrode were examined for copper and nickel-aluminium bronze in a 3.5 wt.% NaCl solution. Mass transfer kinetics for the reduction process studied was compared with rotating disc and cylinder electrode data. The wall-jet electrode mass transfer coefficients for commercially pure copper and cast nickel-aluminium bronze were determined to be 0.01-0.06 cm s^{-1} and 0.01-0.05 cm s^{-1}, respectively.

Keywords: Wall-jet electrode; mass transfer; oxygen reduction; copper; nickel-aluminium bronze.

1. Introduction

Mass transfer in a corrosion process is the transport of species to and from the electrode surface. It plays an important role during flow-induced corrosion where the dissolved oxygen or the dissolved metal-ions must diffuse from the solution to the metal or from the metal to the solution, respectively [1]. The mass transport processes for copper and copper-based alloys have been previously studied using a range of different hydrodynamic systems [2,3]. Hydrodynamic devices use convection to enhance the rate of mass transfer to the electrode surface and offer advantages over techniques that operate in static solutions. Various hydrodynamic devices have been used to study such effects, namely jet impingement electrodes, rotating disc electrodes (RDE) and rotating cylinder electrodes. However, the device used in this present study is a wall-jet electrode (WJE), used to investigate and quantify the electrochemical mechanisms for copper-based alloys during flow-induced corrosion.

The term ‘wall-jet’ was introduced by Glauert [4] to describe when the electrode diameter is larger than the diameter of the nozzle [4-16]. The WJE is a well-characterised hydrodynamic electrode where flow is due to a submerged fluid jet (from a circular nozzle) that impinges at a normal (90°) angle onto a planar disc electrode, with the fluid spreading radial over the electrode surface. The pattern of the flow field and the distinct hydrodynamic regions are

schematically illustrated in Figure 1. The flow field of a wall-jet consists of the following zones: (*i*) the core, where the jet maintains its exit velocity at the centreline while mixing and diffusing with the ambient fluid in its shear layers; (*ii*) the free jet flow, where the core velocity has decayed completely, and the shear layers interact at the jet centrelines, (*iii*) the stagnation region, where the jet changes direction and becomes radially directed and the thickness of the hydrodynamic boundary layer is independent of the radial distance close to the stagnation point and (*iv*) the wall-jet region, a region adjacent to the planar electrode at some distance from the stagnation point where the radial velocity starts to decay and the thickness of the boundary layer increases with radial positions [11]. The wall-jet region is generally considered to begin at approximately three to five nozzle diameters from the stagnation point [17]. The primary flow vector is parallel to the solid surface and the flow profile is characterised by high turbulence intensity, a large velocity gradient at the wall, and high wall shear stress that decreases with increasing distance from the stagnation point [18].

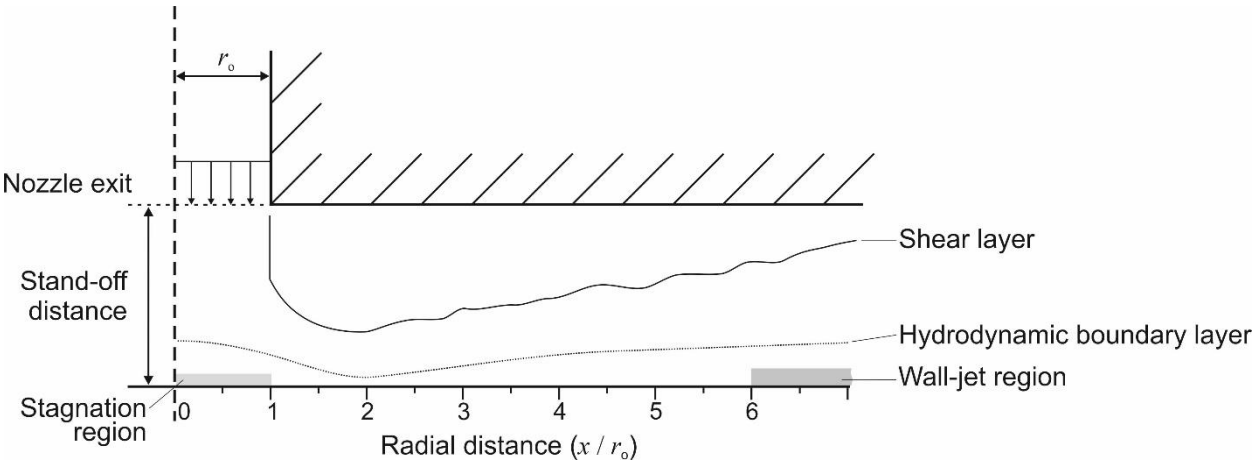

Figure 1: Schematic representation of the wall-jet electrode hydrodynamic regions.

The flow pattern in the wall-jet electrode system has a highly non-uniform flow field across the electrode surface, the rates of mass transport being much higher in the centre of the electrode than at the edge [19]. Hydrodynamic electrodes require an optimised electrode configuration and cell design with well-defined hydrodynamic characteristics, low dead volume, as well as constant effective electrode area, the wall-jet cell fulfils all these requirements [12]. When studying the anodic and cathodic mass transfer kinetics of copper and copper-based alloys it is vitally important to consider the flow regime conditions. Rotating disc electrode rotating cylinder electrode, jet-impingement and wall-jet electrode geometries have all been used as complementary, hydrodynamic working electrodes. The rotating disc and rotating cylinder electrodes provide well-defined surfaces for laminar and turbulent flow studies, respectively. Whereas, the WJE can facilitate a comparison of copper-based alloy dissolution rates under flow corrosion conditions using the less well-controlled and more variable jet impingement

geometry (either free or confined jet, plus nozzle geometry, the stand-off distance between nozzle exit and electrode). In addition, in comparison with the RDE, the WJE assembly has advantages that, firstly arise from the flow-through nature of the device which means that fresh electrolyte is continuously supplied and corrosion products are swept away, as such limiting the build-up of reaction intermediates which might influence the electrode process, and secondly from the high sensitivity of the WJE (compared with RDE) to variations in the rate of mass transport. As with other hydrodynamic electrodes, a limiting current, I_{L}, approach has been used to study the influence of mass transfer within wall-jet electrode. The I_{L} is an important parameter since it represents the maximum rate where current is diffusion limited and can be expressed according to the relationship derived by Yamada and Matsuda [7] for a wall-jet given in Equation (1):

$$I_{\mathrm{L}} = 1.38 z F C_{\mathrm{b}} D^{0.667} \nu^{-0.417} Q^{0.75} d_{\mathrm{n}}^{-0.5} r_{\mathrm{w}}^{0.75} \quad \ldots\ldots (1)$$

where z is the number of electrons involved in the electrode reaction, F the Faraday constant, C_{b} is the bulk concentration, D is the diffusion coefficient, ν is the kinematic viscosity, Q is the volume flow rate, d_{n} is the diameter of nozzle and r_{w} is the radius of the working electrode. Figure 2 shows a schematic of a linear sweep polarisation curve with three distinct regions evident: charge transfer, mixed and mass transport controlled (diffusion limited) [20,21].

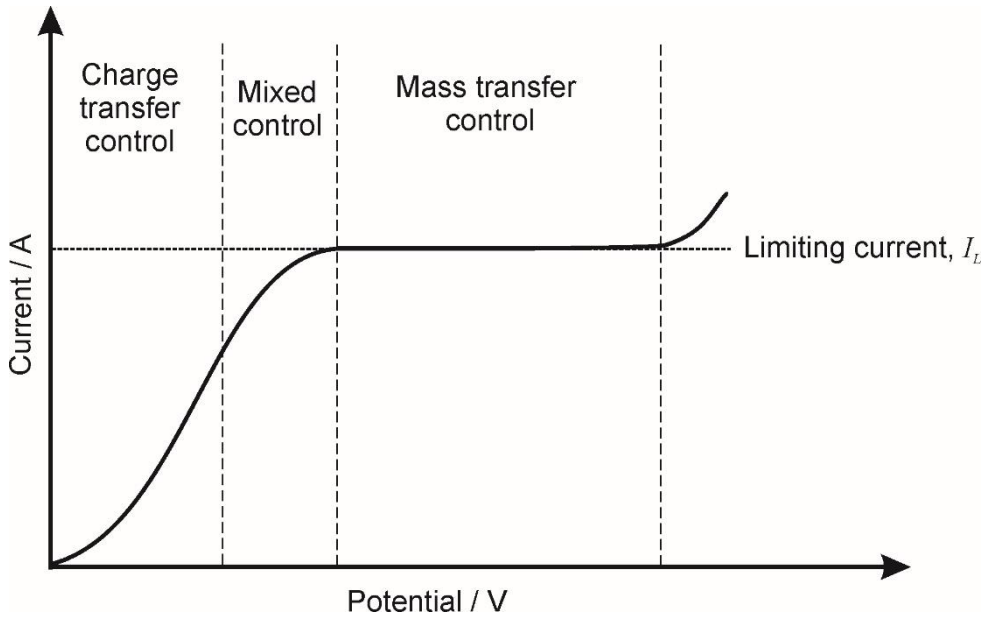

Figure 2: Schematic of a polarisation curve showing the locations of the charge and mass transport control regions.

The 'charge transfer control' region describes the electrode reactions that are limited by the rate of charge transfer at the electrode-solution interface at low applied potentials. The current increases exponentially at more positive applied potentials, which is affected by both applied

potential and the flow rate. This is the 'mixed control' region where a combination of charge and mass transfer processes control the electrode reactions. At high applied potentials, a limiting current occurs, which corresponds to the maximum reaction rate permitted by mass transport. The limiting current technique is a convenient technique for transport-rate studies, since the mass transport coefficient (k_m) can be readily and accurately calculated from the experimentally obtained limiting current using Equation (2) [20,21].

$$k_{\mathrm{m}} = \frac{I_{\mathrm{L}}}{zFAC_{\mathrm{b}}} \quad \ldots\ldots(2)$$

The aim of this study is to determine the cathodic mass transfer kinetics of flow corrosion of commercial purity copper and cast nickel-aluminium bronze (NAB) wall-jet electrodes and to follow on with comparisons of the anodic response, both in aerated 3.5 wt.% NaCl test solutions.

2. Experimental

The WJE was used for the first time to investigate the mass transfer kinetics of flow corrosion. The wall-jet flow cell was supplied by IJ Cambria Scientific Ltd., UK. The flow cell consisted of working electrode disc with a diameter of 3 mm, a silver/silver chloride (Ag/AgCl. 3 M KCl) reference electrode and a platinum (Pt) counter electrode which is also utilised as the out-flow tube from the cell assembly. The inlet jet nozzle diameter was 300 µm with a 350 µm stand-off distance (nozzle exit to working electrode). Figure 3 shows the schematic of the modified WJE. Current interrupt measurements show this design had an ohmic resistance drop of about 80 Ω.

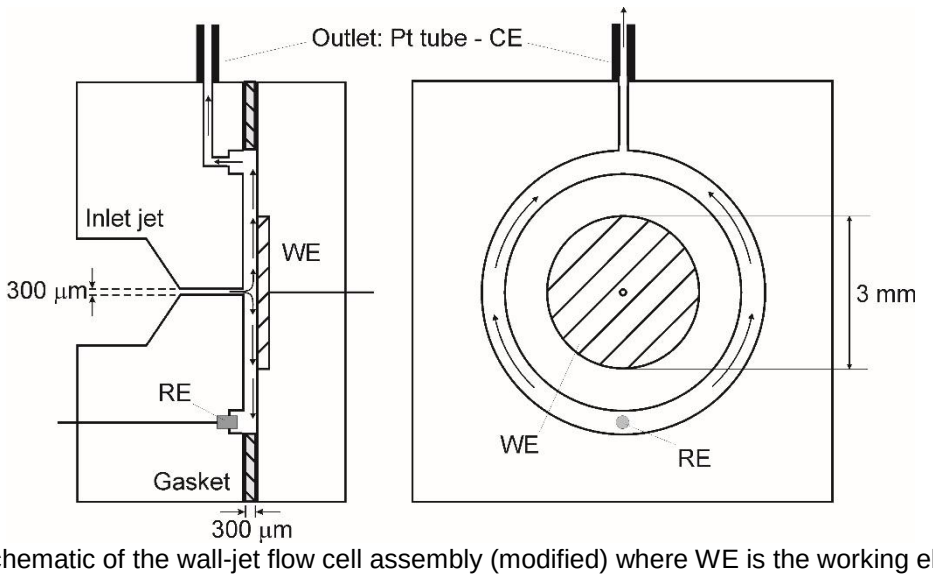

Figure 3: Schematic of the wall-jet flow cell assembly (modified) where WE is the working electrode, CE is the counter electrode and RE the reference electrode).

Electrolyte flow was achieved using a bespoke syringe pump, consisting of two positive displacement syringes with a top and bottom cylinder (piston), each with a capacity of 0.5 L of water and was rack driven. All wetted surfaces of the pump were non-metallic, manufactured from ultra-high molecular weight polyethylene (UHMWPE). The design mimics a dual-syringe pump in that one piston discharges (pumps to the WJE) the test electrolyte, while the other recharges (refilled from an external electrolyte reservoir) and *vice versa*.

Wall-jet electrode calibration

The WJE experiments were calibrated using a hexacyanoferrate ion, $Fe(CN)_6^{4-}$, redox system [22], containing 0.1 mM $K_4Fe(CN)_6$ and 1 M KCl as the supporting electrolyte at 20°C. The Pt electrode surface (diameter: 3 mm) was polished with a 0.3 µm Al_2O_3 slurry and degreased with acetone. Linear sweep voltammetry was carried out on the platinum surface at a sweep rate 1 mV s^{-1} and the corresponding oxidation currents were measured at different flow rates over a range of +0.1 V to +1.3 V *vs.* Ag/AgCl potential. The cell volume flow rates were calibrated over a range from 0.03 cm^3 s^{-1} to 0.33 cm^3 s^{-1} by a simple volumetric-time analysis. A Gamry Instruments PC4-750 potentiostat and DC105 software was used to perform the linear sweep voltammetry. The test solution was deaerated by continuous sparging for 1 h with nitrogen before the test solution was fed into the pump assembly to measure the background current. Prior to filling nitrogen was used to replace the air within the pump assembly.

Mass transfer study

The mass transfer kinetics as a function of volume flow rate (from 0.05 cm^3 s^{-1} to 0.46 cm^3 s^{-1}) were studied for commercially pure copper, Cu (99.99%), and cast nickel-aluminium bronze, NAB (Cu**Al**9**Ni**5**Fe**4**Mn**), in a 3.5 wt.% NaCl test solution. The NAB was supplied by Langley Alloys conforming to British Naval specification NES 747 Part 2 (chemical composition: Al 9.32, Ni 5.38, Fe 5.00, Mn 1.10, Si 0.05% wt. and Cu balance). The copper and NAB specimens (diameter: 3 mm) were wet ground (up to grade 1200 SiC paper) and the final lapping procedure used a 1 µm diamond suspension to achieve a surface finish (R_a) of less than 0.01 µm and degreased with acetone and stored in a desiccator before testing.The reduction reaction kinetics for these copper alloys plays a crucial role and ultimately influences the overall corrosion rate. Thus, the emphasis was the study of the oxygen reduction reaction (ORR) at the freshly polished surfaces of commercially pure copper and NAB. Linear sweep voltammetry was performed to study the ORR at freshly polished specimen surfaces over a –0.200 V to –1.600 V *vs.* Ag/AgCl potential range. The test electrolyte was either continuously aerated or deaerated achieved by continuous sparing with air or nitrogen, respectively. The dissolved oxygen (DO) concentration and electrolyte temperature were measured using a Hanna Instruments HI9145 DO probe during each experiment. These readings are shown in Table 1 along with the cell flow

rates and the nozzle Reynolds (*Re*) numbers. The critical transition between laminar/turbulent flow for a jet, Re_{jet}, is 300 and thus the WJE operated predominately within a well-defined turbulent regime [23].

Table 1: Measured temperature, dissolved oxygen and flow rates for each experimental condition

Experiment	Temperature / °C	DO / ppm	C_{O_2} (×10^{-7}) / mol cm^{-3}	Flow rate / cm^3 s^{-1}	Re_{jet}
Oxygen reduction on CP Cu	22.0 ± 0.1	6.3 ± 0.2	1.96	0.05 to 0.50 ± 0.02	234 to 1956
Oxygen reduction on NAB	18.9 ± 0.2	7.3 ± 0.2	2.27	0.06 to 0.45 ± 0.02	258 to 1892

3. Results and discussion

3.1 Calibration of the wall-jet electrode

The WJE has been calibrated by means of mass transport limited current measurements using the model reaction of the oxidation of the hexacyanoferrate ion on a Pt electrode surface, *i.e.*, the ferro/ferricyanide redox couple.

$$Fe(CN)_6^{4-} \rightarrow Fe(CN)_6^{3-} + e^- \qquad \ldots\ldots(3)$$

The resultant current-voltage curves are shown in Figure 4, for volume flow rates between 0.03 cm^3 s^{-1} and 0.33 cm^3 s^{-1} (jet velocity between 0.4 m s^{-1} to 4.8 m s^{-1}). The background scan was obtained at a zero flow rate.

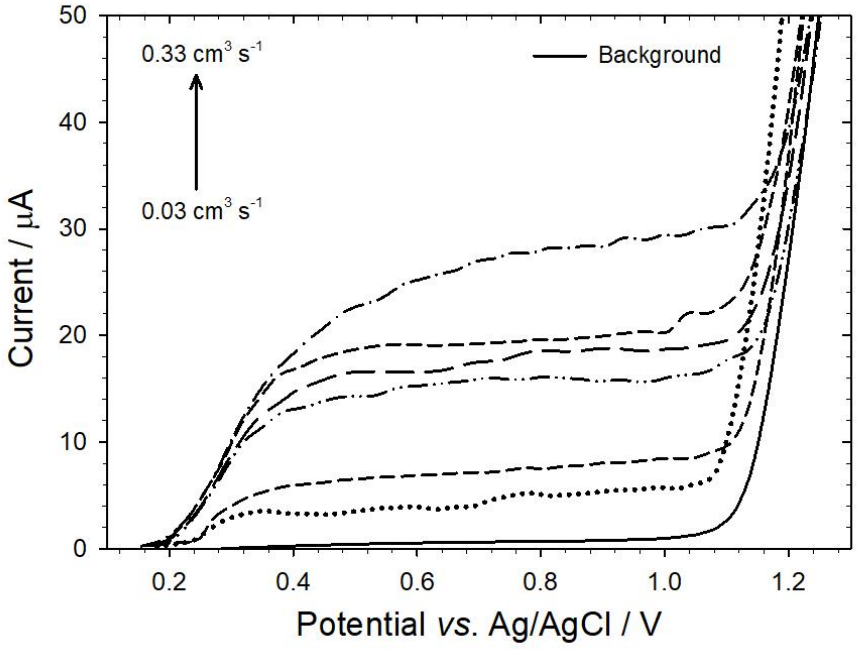

Figure 4: The limiting current plateau region for a 0.1 mM $K_4Fe(CN)_6$ and 1 M KCl solution at a platinum electrode (diameter: 3 mm) for a sweep rate of 1 mV s^{-1} at 20°C and velocities ranging from 0.4 to 4.8 m s^{-1}.

Well-defined reduction waves were obtained for the wall jet electrode, although the limiting diffusion currents show some fluctuations. As the voltage is swept in the positive direction, the current initially increases but then plateaus out until approximately +1.1 V *vs*. Ag/AgCl where oxygen evolution occurs. The plateau represents the limiting current for the redox species. The limiting current was obtained by fitting a horizontal line for current points between +0.4 V and +1.0 V *vs*. Ag/AgCl and subtracting the background response. Figure 5 shows a plot of limiting current against the volume flow rate with the exponent of 0.75. The limiting current for the redox reaction according to Yamada and Matsuda [7] is given by Equation (4).

$$I_{\mathrm{L}} = 1.38zF[\mathrm{Fe(CN)}_6^{4-}]D^{0.667}\nu^{-0.417}Q^{0.75}d_{\mathrm{n}}^{-0.5}r_{\mathrm{w}}^{0.75} \qquad \ldots\ldots(4)$$

where z = 1, F = 96485 A s mol^{-1}, $\mathrm{Fe(CN)}_6^{4-}$ = 0.1×10^{-6} mol cm^{-3}, ν = 0.01 cm^2 s^{-1}, r_{w} = 0.15 cm, and d_{n} = 0.03 cm.

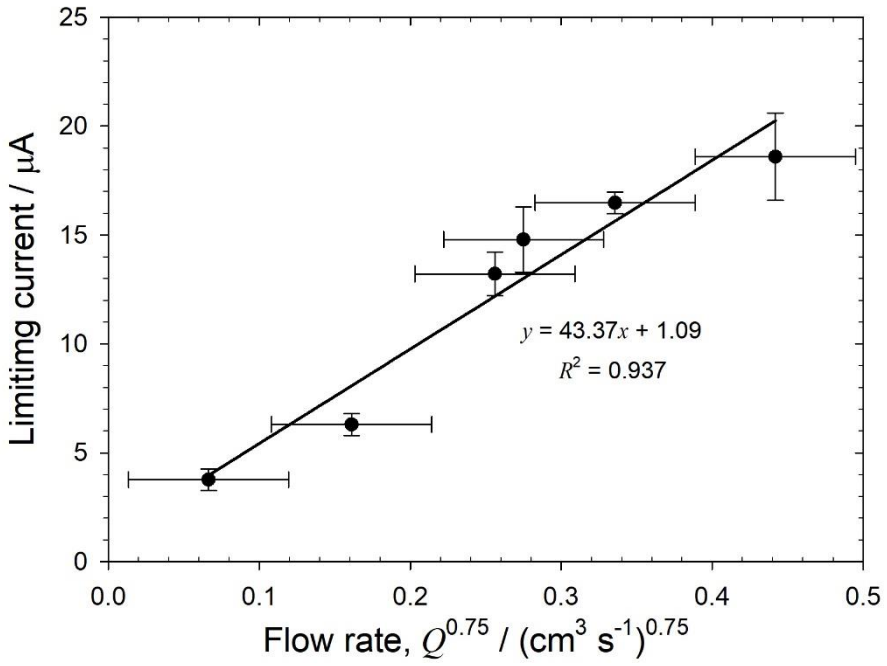

Figure 5: Limiting diffusion current *vs*. flow rate for a 0.1 mM $K_4Fe(CN)_6$ and 1M KCl solution at a platinum electrode (diameter: 3 mm) at 20°C.

The slope obtained was used to calculate the diffusion coefficient of the hexacyanoferrate ion by using Equation (4). The diffusion coefficient was calculated to be 6.7×10^{-6} cm^2 s^{-1}. This compares well with the diffusion coefficients found in the published literature, *i.e.*, 6.5×10^{-6} to 7.1×10^{-6} cm^2 s^{-1} for RDE and RCE geometries [7,24-26].

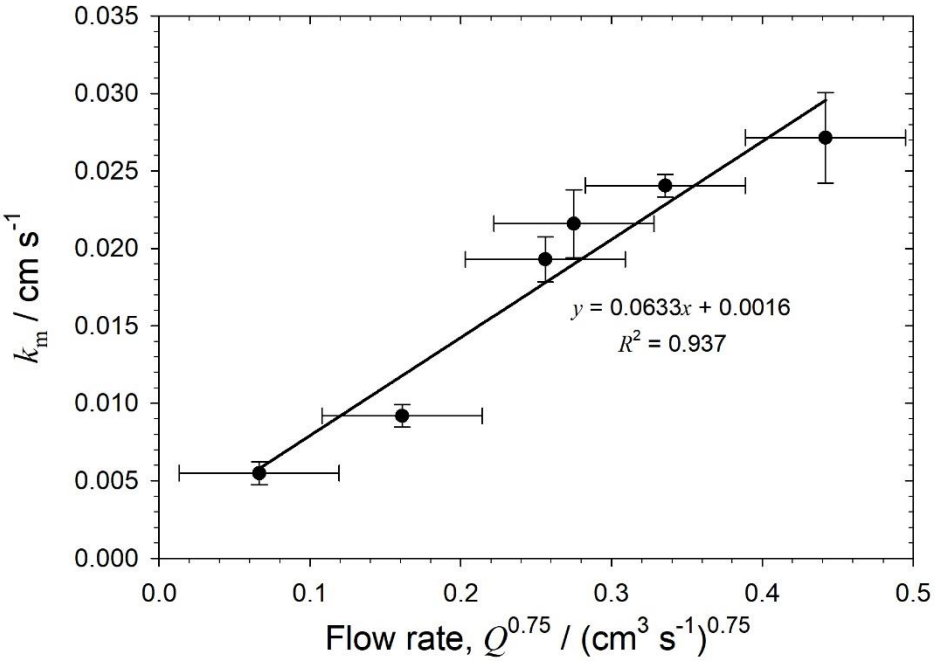

Figure 6: Mass transfer coefficient for hexacyanoferrate ions at 20ºC.

Figure 6 shows the mass transfer coefficients using the values of diffusion coefficients for hexacyanoferrate ions and Equation (2), the mass transfer coefficient, k_m, was plotted as a function of $Q^{0.75}$. Mass transfer coefficients of approximately 0.01 cm s^{-1} to 0.03 cm s^{-1} were calculated. The plot of limiting current against the flow rate confirms the linear relationship predicted by the Yamada and Matsuda for the WJE. Thus, the WJE cell assembly used in this study has been shown to be suitable for carrying out the mass transfer studies.

3.2 Mass transfer of dissolved oxygen

The results of the mass transfer of oxygen to the reduction reaction on copper and NAB surfaces within the wall jet flow cell are discussed in this section. Figures 7 and 8 show oxygen reduction at copper (Cu) and NAB electrodes in a 3.5 wt.% NaCl solution, respectively. Oxygen reduction is the predominant cathodic reduction for potentials more positive than –1.5 V *vs*. Ag/AgCl. The cathodic polarisation curves for Cu and NAB show single wave responses for oxygen reduction which indicates an overall four-electron exchange. The wave indicates the reaction is charge-transfer controlled at low cathodically applied potentials close to –0.3 V. At more negative potentials, the reaction is under mixed-control. For further increases of potential, *i.e.,* between –0.6 V to –1.5 V, the current is approximately constant. This is the limiting current at which oxygen reduction is under mass transport/diffusion control. The limiting current increases with increasing flow rate due to greater mass-transport of oxygen to the electrode surface. Hydrogen evolution predominates at potentials more negative than –1.5 V *vs*.

Ag/AgCl. The background scan was obtained at zero flow rate after removal of oxygen by nitrogen sparging.

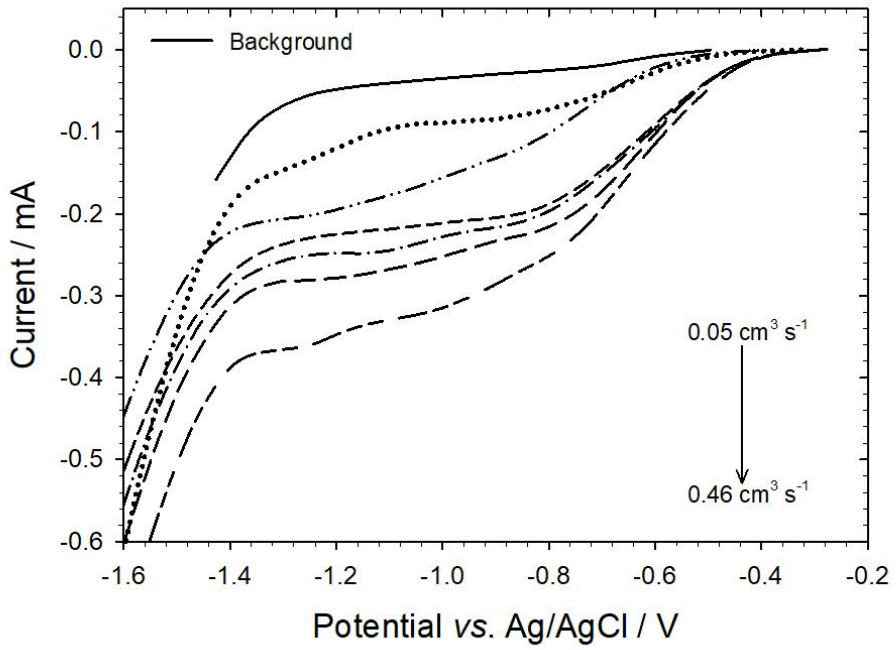

Figure 7: Cathodic polarisation curves for oxygen reduction at the copper wall-jet electrode in a 3.5 wt.% NaCl solution at 22°C and velocities ranging from 0.7 m s^{-1} to 6.5 m s^{-1}.

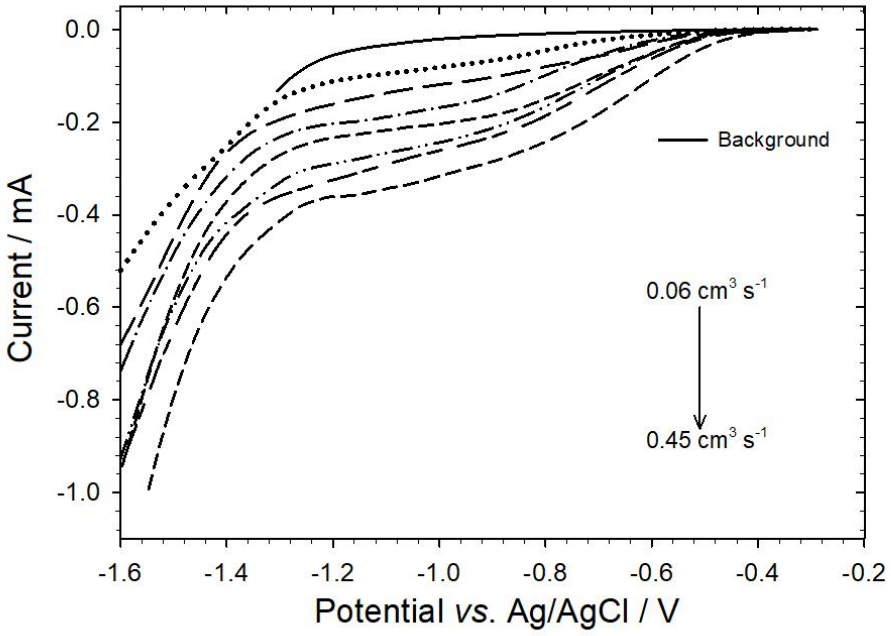

Figure 8: Cathodic polarisation curves for oxygen reduction at the NAB wall-jet electrode in a 3.5 wt.% NaCl solution at 19°C and velocities ranging from 0.8 m s^{-1} to 6.3 m s^{-1}.

The limiting current data was obtained using the curve fitting method as outlined by Ponce-de-Leon and Field [27] by plotting log (E/I) against reciprocal current log ($1/I$), see Figure 9. Accordingly, if the current $I = f(E)$ then,

$$\frac{d\left(\frac{E}{I}\right)}{d\left(\frac{1}{I}\right)} = \frac{d\left(\frac{E}{I}\right)}{d(I)} \times \frac{d(I)}{d\left(\frac{1}{I}\right)} \qquad \ldots\ldots(5)$$

$$= -I^2\left[\left(\frac{1}{I}\right) \times \frac{d(E)}{d(I)} - \frac{E}{I^2}\right]$$

$$= -I\left[\left(\frac{d(I)}{d(E)}\right)^{-1} - \frac{E}{I}\right] \qquad \ldots\ldots(6)$$

The term in square brackets increases when the change of current (I) relative to changes in potential (E) decreases, *i.e.,* as the condition of limiting current are approached. Under these conditions, the curve in an E/I against $1/I$ plot is very steep. Ideally, a limiting current would correspond to $d(I)/d(E) = 0$, and so the upward curve in the E/I against $1/I$ would be vertical. Under certain experimental conditions this is masked by a second reaction or by an IR drop and so the determination of the condition corresponding to mass transfer limitation has been taken to be the mid-point between the maximum and minimum point in the E/Iagainst$1/I$ curve, see Figure 9. The average of these two values gives a limiting current at the point of inflection. Figures 10 and 11 show the limiting current *vs*. flow rates for Cu and NAB, respectively.

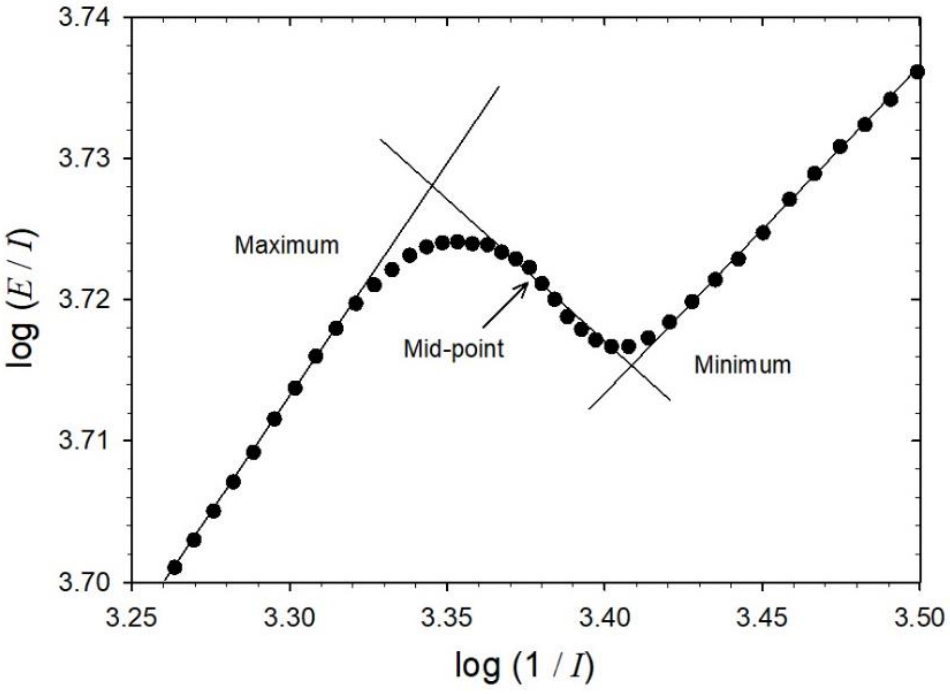

Figure 9: Limiting current determination, after [27].

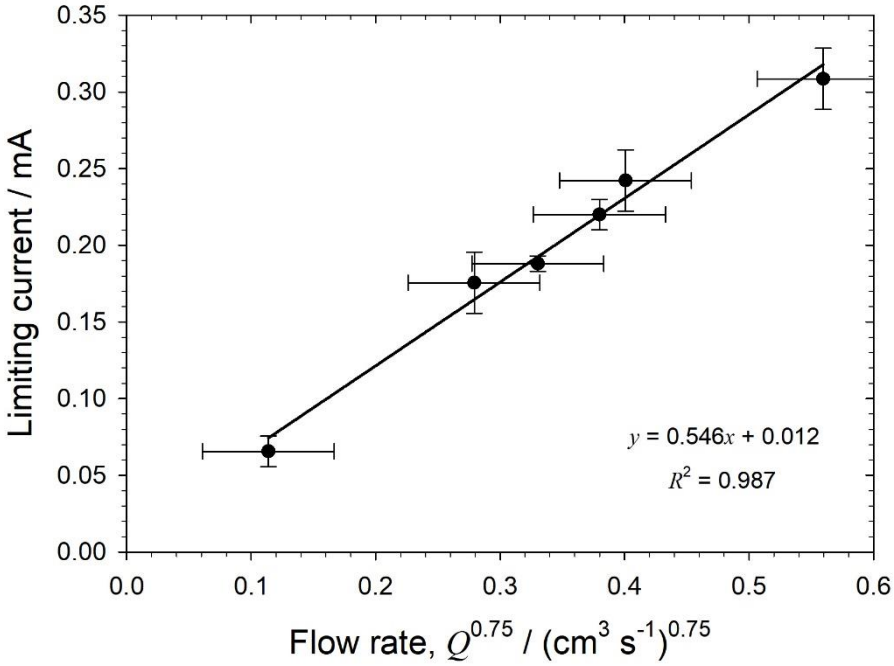

Figure 10: Limiting current *vs*. flow rate plot for the oxygen reduction reaction at the copper wall-jet electrode using a 3.5 wt.% NaCl solution at 22°C.

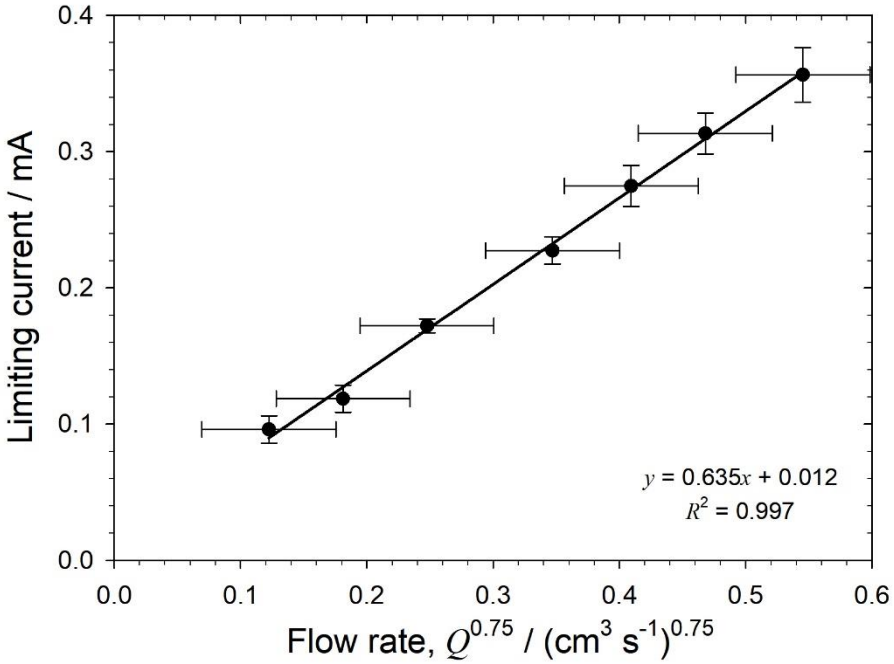

Figure 11: Limiting current *vs*. flow rate plot for the oxygen reduction reaction at the NAB wall-jet electrode using a 3.5 wt.% NaCl solution at 18.9ºC.

The coefficient of diffusion was calculated for Cu and NAB at 22.0°C and 18.9°C and are shown in Table 2, respectively.

$$I_{\mathrm{L}} = 1.38 z F C_{\mathrm{O_2}} D_{\mathrm{O_2}}^{0.667} \nu^{-0.417} Q^{0.75} d_{\mathrm{n}}^{-0.5} r_{\mathrm{w}}^{0.75} \quad \ldots\ldots (7)$$

where $C_{\mathrm{O_2}}$ is the bulk concentration and $D_{\mathrm{O_2}}$ is the diffusion coefficient of dissolved oxygen.

Table 2: Calculated oxygen coefficient of diffusion for pure copper and NAB in a WJE

Material	D_{O_2} / (×10^{-5} cm^2 s^{-1})	Temperature / °C
Cu	1.30 ± 0.10	22.0
NAB	1.31 ± 0.05	18.9

The wall-jet derived diffusion coefficient for oxygen has been compared with values quoted in the literature that have been obtained for copper-based alloys at 25°C, see Table 3. The diffusion coefficient at 25°C has been derived using Equation 8 [28].

$$D_{25} = D_{\mathrm{o}} \cdot \exp\left[\frac{-E_{\mathrm{a}}}{R}\left(\frac{1}{T_{25}} - \frac{1}{T_{\mathrm{o}}}\right)\right] \quad \ldots\ldots(8)$$

Where D_{o} is the diffusion coefficient at the experimental temperature, T_{o}, R is the gas constant 8.314 J^{-1} K^{-1} mol^{-1}, E_{a} is the activation energy for diffusion of oxygen which is 83 J mol^{-1} [28] and T_{25} is the temperature at 25°C.

Table 3: Diffusion coefficients corrected to 25°C from the literature and the present work

Electrode material	Cell geometry	Test electrolyte	C_{O_2} / (×10^{-7}) mol cm^{-3}	D_{25} / (×10^{-5}) cm^2 s^{-1}	Ref.
Cu	Rectangular channel cell	Natural seawater	1.85	1.6	[29]
Cu-30Ni	Rectangular channel cell	Natural seawater	1.85	1.6	[29]
Cu	RDE	Filtered seawater	2.16	2.0	[30]
Cu	RDE	Artificial seawater	2.19	2.2	[30]
Cu-10Ni	RDE	Filtered seawater	2.16	2.3	[30]
Cu-10Ni	RDE	Artificial seawater	2.19	2.7	[30]
NAB (wrought)	RDE	Filtered seawater	2.16	1.7	[30]
NAB (wrought)	RDE	Artificial seawater	2.19	1.8	[30]
Cu-Ni	RDE	1 mol L^{-3} NaCl	2.00	1.8	[31]
Cu	RDE	1 mol L^{-3} NaCl	2.00	1.8	[32]
Cu	RDE	0.5 mol L^{-3} NaCl	2.00	2.0	[33]
Cu	WJE	0.6 mol L^{-3} NaCl	1.96	1.4	–
NAB (cast)	WJE	0.6 mol L^{-3} NaCl	2.27	1.4	–

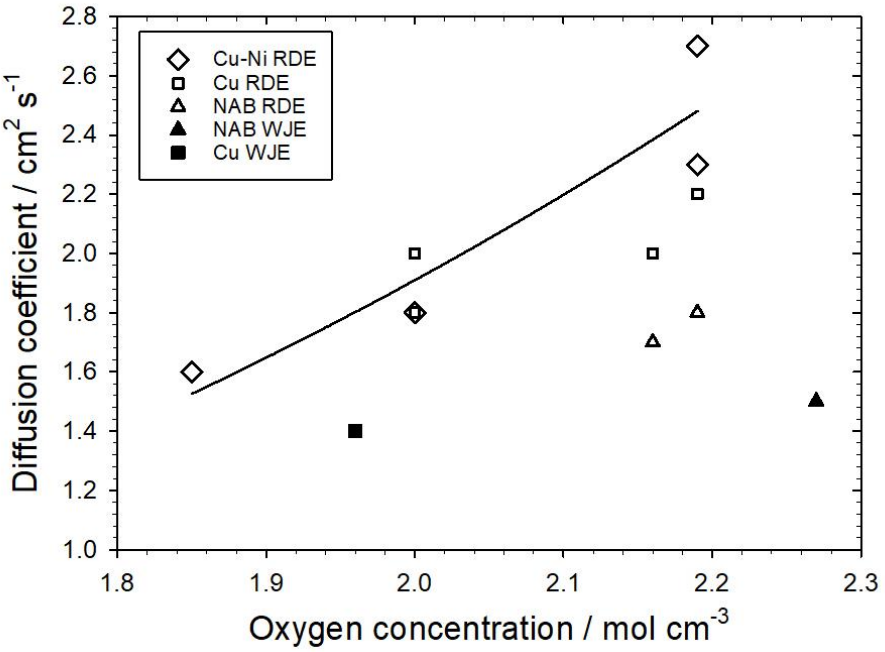

Figure 12: Comparison of the oxygen diffusion coefficient for copper-based alloys in different flow cell geometries.

In Table 3 a mean diffusion coefficient for oxygen reduction on Cu and Cu-Ni found in the open literature ranges from 1.6×10^{-5} to 2.7×10^{-5} cm^2 s^{-1}, with an average of about 2.0×10^{-5} cm^2 s^{-1}. This average is higher than experimental values obtained in WJE by about 40%. The low diffusion coefficient for the WJE relative to those for RDE is most likely to be related to the cell geometry and the highly non-uniform flow field that is established in the cell, with enhanced effects at radial distances close to the stagnation zone immediately adjacent to the nozzle exit. Thus, influencing the net mass transport within the presence of a concentration gradient (the WJE concentration gradient will be geometrical constrained and electrolyte well mixed within the 300 μm wide wall-jet channel). Figure 12 shows that quoted values of D increases with increasing oxygen concentration. According to Nernst-Einstein, the diffusion coefficient (D) of oxygen D_{O_2}increases with increasing molar conductivity (λ) of oxygen given by Equation (9) [34].

$$D = \frac{R_o T \lambda}{z^2 F^2} \qquad \ldots\ldots(9)$$

The molar conductivity of oxygen for a strong electrolyte (3.5 wt.% NaCl solution), according to Kohlrausch's law [34], is proportional to the concentration of oxygen, C_{O_2} given by the Equation (10):

$$\lambda = \lambda_o - k\sqrt{C_{O_2}} \quad \ldots\ldots (10)$$

Where λ_o molar conductivity at infinite dilution, and k is the coefficient depending on electrolyte.

The Equations 9 and 10 show a relationship between diffusion coefficient and concentration *i.e.,* $D \propto \sqrt{C_{O_2}}$. The expression $\sqrt{C_{O_2}}$ tends to zero as the concentration of oxygen in the solution decreases and D becomes negligible, *i.e*., the Nernst–Einstein Equation (9) becomes increasingly valid for the increasing dilution of the oxygen in solution [34]. However, Figure 12 shows the concentration exponent is greater than 0.5, *i.e*., $D \approx C_{O_2}^2$ for the present study, possibly due to the higher concentration of oxygen.

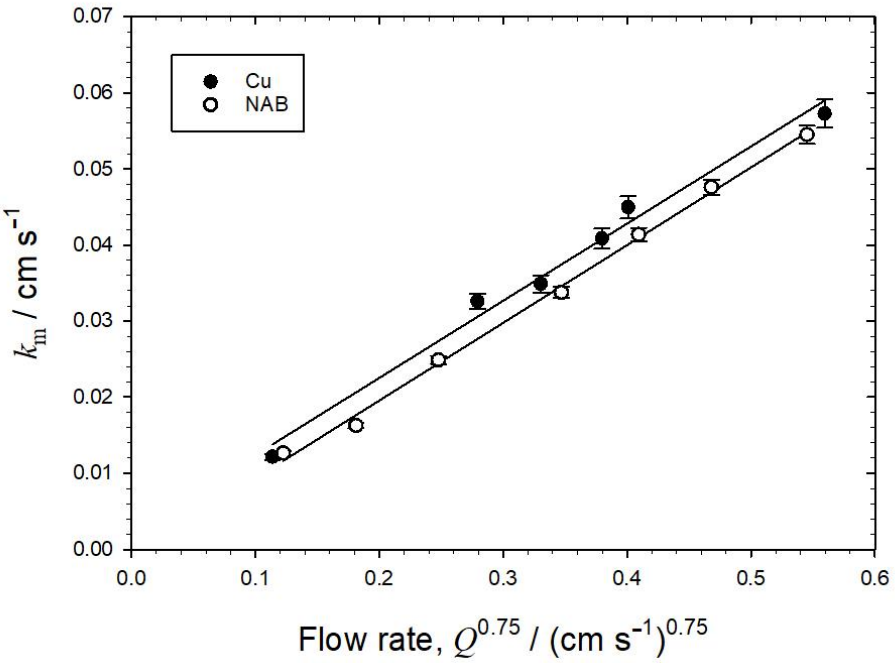

Figure 13: Plots of mass transfer coefficient for oxygen reduction on copper and NAB.

The mass transfer coefficients calculated using Equation (2) and using the diffusion coefficient of the WJE from Table 2 are plotted as a function of flow rate and shown in Figure 13. Excellent agreement is seen between the Cu and NAB results. Table 4 compares the mass transfer coefficients for oxygen reduction on freshly polished copper and NAB in 3.5 wt.% NaCl solutions derived from wall-jet, rotating disc and cylinder electrodes. The range of mass transfer coefficients obtained with the wall-jet is relatively high compared to the other hydrodynamic geometries. This can be related to the higher turbulence intensity that occurs within the WJE which results in enhanced dissolved oxygen mass transfer to the electrode surfaces. This has important implications for the corrosion kinetics and the formation of oxide films, both in terms of the mechanical influence of turbulence intensity and flow corrosion effects, plus the availability

of oxygen at the electrode surface to enhance formation of protective oxide films within a given flow condition.

Table 4: Comparison of mass transfer coefficients for oxygen in different cell geometries at 25°C

Electrode material	Flow cell geometry	k_m / cm s^{-1}
Cu	WJE	0.010 – 0.060
Cu	RDE [30]	0.005 – 0.030
Cu	RCE [30]	0.003 – 0.010
NAB	WJE	0.010 – 0.050

4. NAB anodic polarisation performance in a WJE

As discussed previously, oxygen reduction kinetics play an important role in controlling corrosion; however, it is equally crucial to assess the anodic kinetics as well. The aim of this aspect of the study was to compare the anodic polarisation performance of NAB with that from other commonly used hydrodynamic electrode assemblies. Figure 14 shows the polarisation of NAB in the different cell geometries used within this study. By analogy with copper [19,21,32,35-40], it has been well-established that the initial corrosion process for NAB in aerated chloride media is the anodic interfacial dissolution of copper to form a dichlorocuprous anion complex, which can be simplified to:

$$Cu + 2Cl^- \rightleftharpoons CuCl_2^- + e^- \quad \text{.....(11)}$$

It has been reported that at chloride concentrations of 10 mM to 1 M that $CuCl_2^-$ is the predominant complex [41,42]. In neutral solutions the presence of high concentrations of $CuCl_2^-$ at the metal surface may result in a hydrolysis reaction and the formation of Cu_2O according to:

$$2CuCl_2^- + H_2O \rightleftharpoons Cu_2O + 2H^+ + 4Cl^- \quad \text{.....(12)}$$

Or alternatively, the CuCl produced by the precipitation of dissolved Cu(I) in a chloride media may lead to further Cu_2O growth:

$$2CuCl + H_2O \rightleftharpoons Cu_2O + 2H^+ + 2Cl^- \quad \text{.....(13)}$$

The anodic polarisations of commercial purity copper and NAB under static immersion show typical regions of 'apparent Tafel' behaviour (mixed charge transfer and mass transport controlled kinetics), a pseudo passivation region with oxide film formation leading to a maximum peak current density (plus, the possibility of surface precipitation of CuCl) that is followed by a 'limiting' current density linked to film or further metal dissolution, and increase of current density due to the formation cupric species as reported in the literature [21,30]. However, the WJE response differs from the RDE and static immersion test. The anodic kinetics in both the WJE and JIR are subject to a flow-through system and thus show a different response when

compared with the static tests (no hydrodynamic flow) or RDE, which have confined volumes of electrolyte. It is evident from Figure 14 that there is a definite change in the mechanism of anodic polarisation (and subsequent nature of any protective film formation) for WJE and JIR. The formation of intermediate species such as $CuCl_2^-$ will be swept away with the flow steam crucially limiting the formation of Cu_2O films, thus preventing an elementary step in protective oxide film development that NAB is chiefly reliant on when in-service. Nonetheless, for Cu–Al alloys such as NAB, in the absence of hydrolysis of Cu(I) species, alumina (Al_2O_3) is likely to predominate within the nascent oxide film, which is impermeable to the passage of cuprous cations and thus sustains a lower copper dissolution rate. The WJE setup can provide key mechanistic insights into the copper and NAB flow corrosion processes, across static to 6.3 m s^{-1} impinging fluid jet conditions, particularly the influence of controlled laminar and turbulent hydrodynamic conditions on the dissolution kinetics that may better represent in-service exposures.

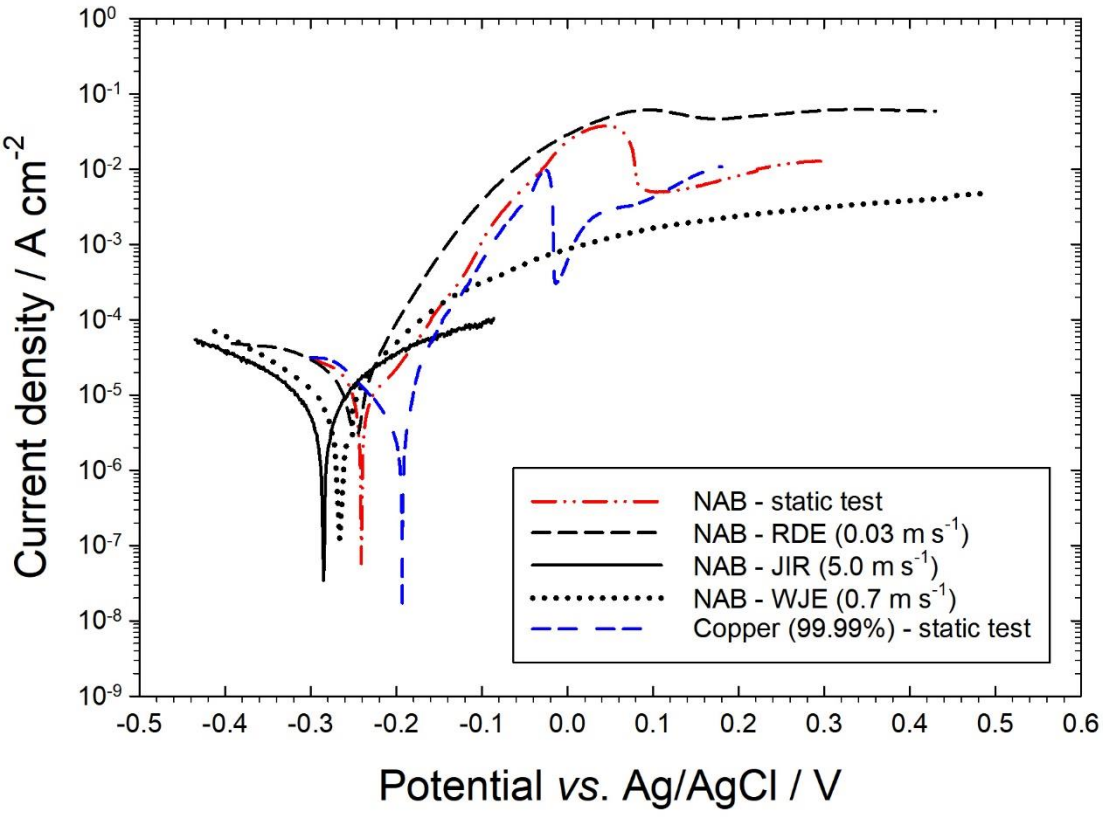

Figure 14: NAB anodic polarisation using various flow cell geometries. The test electrolyte was aerated 3.5 wt.% NaCl solution at 20°C.

5. Conclusions

This work used an innovative investigation into the corrosion performance and mass transfer kinetics in a wall-jet electrode for freshly polished commercially pure copper and nickel-aluminium bronze. Quantitative cathodic kinetics data that influence the corrosion performance was obtained using a limiting current technique. The cathodic reactions for copper and NAB were dominated by the oxygen reduction. The WJE electrochemical performance differed from either the rotating disc or cylinder electrode geometries, *e.g.*, markedly lower diffusion coefficients for oxygen were obtained for the WJE due to the flow-through cell geometry and constrained flow field effects. The higher mass transfer coefficients for oxygen reduction on copper and NAB surface in the WJE compared to rotating disc and cylinder are due to the greater turbulence intensity within the thin channel. WJE electrolyte flow-through prevents secondary hydrolysis of Cu(I) species and Cu_2O film formation allowing flow corrosion performance to be characterised with a continually refreshed test solution.

6. Acknowledgements

The authors acknowledge the financial support of the Defence Science and Technology Laboratory (Dstl) and Dr Clive Tuck from Langley Alloys.

7. References

1. GH Sedahmed, MSE Abdo, M Amer, G Abd El-Latif, Mass transfer at a pipe inlet zone in relation to impingement corrosion, *Int. Commun. Heat Mass* 1998, 443-451. https://doi.org/10.1016/S0735-1933(98)00031-1
2. JA Wharton, RC Barik, RJK Wood, KR Stokes, G Kear, FC Walsh, The corrosion of nickel-aluminium bronze in seawater, *Corros Sci.* 47 (2005) p. 3336-3367. doi: doi:10.1016/j.corsci.2005.05.053
3. *FC Walsh*, G Kear, AH Nahlé, JA Wharton, LF Arenas, The rotating cylinder electrode for studies of corrosion engineering and protection of metals – a critical review, *Corros. Sci*. 123 (2017) pp. 1-20. http://dx.doi.org/10.1016/j.corsci.2017.03.024
4. MB Glauret, The wall-jet, *J. Fluid. Mech*. 1 (1956) 625-631.
5. Y Nishiki, K Aoki, K Tokuda, H Matsuda, Secondary current distribution in a two-dimensional model cell composed of an electrode with an open part, *J. Appl. Electrochem*. 16 (1986) 291-303. https://doi.org/10.1007/BF01093363
6. WJ Albery, CMA Brett, Wall-jet ring-disc electrode: Part I. Theory, *J. Electroanal. Chem*. 148 (1983) 211-220. https://doi.org/10.1016/S0022-0728(83)80396-9
7. J Yamada, H Matsuda, Limiting diffusion currents in hydrodynamic voltammetry III. Wall-jet electrodes, *J. Electroanal. Chem.* 44 (1973) 189-198. https://doi.org/10.1016/S0022-0728(73)80245-1
8. H. Gunasingham, B Fleet, Wall-jet electrode in continuous monitoring voltammetry, *Anal. Chem*. 55 (1983) 1409-1414. DOI:10.1021/ac00259a050
9. WJ Albery, ML Hitchman, Ring disc electrodes, Oxford University Press, Oxford, 1971. ISBN 10: 0198553498
10. WJ Albery, The current distribution on a wall-jet electrode, *J. Electroanal. Chem*.191 (1985) 1-13. https://doi.org/10.1016/S0022-0728(85)80002-4
11. A Göransson,C Trägårdh, An experimental study of the kinetics of particle deposition in a wall-jet cell using total internal reflection microscopy, *J. Colloid. Interf. Sci*.231 (2000) 228-237. DOI: 10.1006/jcis.2000.7139

12. RG Compton, AC Fisher, GP Tyley, Non-uniform accessibility and the use of hydrodynamic electrodes for mechanistic studies: a comparison of wall-jet and rotating disc electrodes, *J. Appl. Electrochem*. 21 (1991) 295-300. DOI: 10.1007/BF01020211
13. CMA Brett, AM Oliveira Brett, LC Mitoseriu, Amperometric batch injection analysis: Theoretical aspects of current transients and comparison with wall-jet electrodes in continuous flow, *Electroanalysis* 7 (1995) 225-229. https://doi.org/10.1002/elan.1140070305
14. LT Di Benedetto, T Dimitrakopoulos, Evaluation of a new wall-jet flow-through cell for commercial ion-selective electrodes in flow injection potentiometry, *Electroanalysis* 9 (2005), 179-182. https://doi.org/10.1002/elan.1140090219
15. B Soucaze-Guillous, W Kutner, Flow characteristics of a versatile wall-jet or radial-flow thin-layer large-volume cell for electrochemical detection in flow-through analytical systems, *Electroanalysis* 9 (1997) 32-39. https://doi.org/10.1002/elan.1140090109
16. MJ Kimlinger and RS Martin, The Use of a 3D-Printed Microfluidic Device and Pressure Mobilization for Integrating Capillary Electrophoresis with Electrochemical Detection, *Electroanalysis*, 30 (2018) 2241-2249. https://doi.org/10.1002/elan.201800367
17. PR Roberge, Erosion-Corrosion, Chapter 3, in:Corrosion Testing Made Easy series, NACE International, Houston USA 2004.
18. F Giralt, O Trass, Mass transfer from crystalline surfaces in a turbulent impinging jet. Part 2: Erosion and diffusional transfer, *Can. J. Chem. Eng*. 54 (1976) 148-155. https://doi.org/10.1002/cjce.5450540305
19. F King, CD Litke, MJ Quinn, DM LeNeveu, The measurement and prediction of the corrosion potential of copper in chloride solutions as a function of oxygen concentration and mass-transfer coefficient, *Corros. Sci*. 37 (1995) 833-851. https://doi.org/10.1016/0010-938X(95)80013-1
20. D Pletcher, A First Course in Electrode Processes, The Electrochemical Consultancy, Romsey, UK, 1991.
21. G Kear, BD Barker, FC Walsh, Electrochemical corrosion of unalloyed copper in chloride media -a critical review, *Corros. Sci*. 46 (2004) 109-135.https://doi.org/10.1016/S0010-938X(02)00257-3
22. KR Kneten, RL McCreery, Effects of redox system structure on electron-transfer kinetics at ordered graphite and glassy carbon electrodes, *Anal. Chem*. 64 (1992) 2518-2524. DOI: 10.1021/ac00045a011
23. AA Townsend, Turbulence, Chapter 10, in V. Streeter, Handbook of Fluid Dynamics, McGraw-Hill, 1961.
24. JV Macpherson, S Marcar, PR Unwin, Microjet Electrode: A hydrodynamic ultramicroelectrode with high mass transfer rates, *Anal. Chem*. 66 (1994) 2175-2179. DOI: 10.1021/ac00085a037
25. JP Lorimer, B Pollet, SS Phull, TJ Mason, DJ Walton, U Geissler, The effect of ultrasonic frequency and intensity upon limiting currents at rotating disc and stationary electrodes, *Electrochimica Acta* 41 (1996) 2737-2741. DOI: 10.1016/0013-4686(96)00130-2
26. RG Compton, AC Fisher, MH Latham, CMA Brett, A-MCF Oliveira Brett, Wall jet electrode linear sweep voltammetry, *J. Phys. Chem*. 96 (1992) 8363-8367. DOI: 10.1021/j100200a028
27. C Ponce-de-León, RW Field, On the determination of limiting current density from uncertain data, *J. Appl. Electrochem*. 30 (2000) 1087-1090. DOI: 10.1023/A:1004015617522
28. MV Vazquez, SR De Sanchez, EJ Calvo, DJ Schiffrin, The electrochemical reduction of oxygen on polycrystalline copper in borax buffer*, J. Electroanal. Chem*. 374 (1994) 189-197. https://doi.org/10.1016/0022-0728(94)03342-0
29. RJK Wood, SP Hutton, DJ Schiffrin, Mass transfer effects of non-cavitating seawater on the corrosion of Cu and 70Cu-30Ni, *Corros. Sci*. 30 (1990) 1177–1201. https://doi.org/10.1016/0010-938X(90)90198-E
30. G Kear, Electrochemical corrosion of marine alloys under flowing conditions, PhD thesis, University of Portsmouth, 2001.

31. SR De Sanchez, DJ Schiffrin, Use of high speed rotating disc electrodes for the study of erosion-corrosion of copper base alloys in seawater, *Corros. Sci*. 28 (1988) 141–151.https://doi.org/10.1016/0010-938X(88)90091-1
32. F King, MJ Quinn, CD Litke, Oxygen reduction on copper in neutral NaCl solution, *J. Electroanal. Chem*. 385 (1995) 45-55. https://doi.org/10.1016/0022-0728(94)03705-8
33. C Deslouis, B Tribollet, G Mengoli, M Musiani, Electrochemical behaviour of copper in neutral aerated chloride solution. I. Steady-state investigation, *J. Appl. Electrochem.*18 (1988) 374–383. https://doi.org/10.1007/BF01093751
34. JOM Bockris, AKN Reddy, Modern Electrochemistry, 2nd ed., London, 2000.
35. HP Lee, KNobe, Kinetics and mechanisms of Cu electrodissolution in chloride media, *J. Electrochem. Soc*. 133 (1986) 2035-2043. doi: 10.1149/1.2108335
36. AL Bacarella, JC Griess, The anodic dissolution of copper in flowing sodium chloride solutions between 25° and 175°C, *J. Electrochem. Soc*. 120 (1973) 459-465. doi: 10.1149/1.2403477
37. A Moreau, Etude du mecanisme d'oxydo-reduction du cuivre dans les solutions chlorurees acides – I. Systeme Cu-$CuCl_2^-$ *Electrochimica Acta*, 26 (1981) 497-504. https://doi.org/10.1016/0013-4686(81)87029-6
38. B Tribollet, J Newman, Impedance model for a concentrated solution - Application to the electrodissolution of copper in chloride solutions*, J. Electrochem. Soc.* 131 (1984) 2780-2785. doi: 10.1149/1.2115407
39. WH Smyrl, Digital impedance for faradaic analysis - II. Electrodissolution of Cu in HCl, *J. Electrochem. Soc.* 132 (1985) 1555-1562. doi: 10.1149/1.2114164
40. G Bianchi, G Fiori, P Longhi, F Mazza, "Horse Shoe" Corrosion of Copper Alloys in Flowing Sea Water: Mechanism, and Possibility of Cathodic Protection of Condenser Tubes in Power Stations, *Corrosion* 34 (1978) 396-406. DOI: 10.5006/0010-9312-34.11.396
41. M Wang, Y Zhang, M Muhammed, Critical evaluation of thermodynamics of complex formation of metal ions in aqueous solutions III. The system Cu(I,II)−Cl^-−e at 298.15 K, *Hydrometallurgy* 45 (1997) 53-72. https://doi.org/10.1016/S0304-386X(96)00074-6
42. Z Xiao, CH Gammons, AE Williams-Jones, Experimental study of copper(I) chloride complexing in hydrothermal solutions at 40 to 300°C and saturated water vapor pressure, *Geochim. Cosmochimica Acta* 62 (1998) 2949-2964. https://doi.org/10.1016/S0016-7037(98)00228-2